chemistry

MDPI

Article

Using Imidazolium in the Construction of Hybrid 2D and 3D Lead Bromide Pseudoperovskites

Gonzalo García-Espejo [1], Konstantis F. Konidaris [1,*], Antonietta Guagliardi [2] and Norberto Masciocchi [1,*]

[1] Dipartimento di Scienza e Alta Tecnologia and To.Sca.Lab, Università dell'Insubria, Via Valleggio 11, 22100 Como, Italy; gonzalo_ge@outlook.com
[2] Istituto di Cristallografia and To.Sca.Lab, Consiglio Nazionale delle Ricerche, Via Valleggio 11, 22100 Como, Italy; antonella.guagliardi@ic.cnr.it
* Correspondence: konstantis.konidaris@uninsubria.it (K.F.K.); norberto.masciocchi@uninsubria.it (N.M.)

Abstract: The field of hybrid organic–inorganic perovskite materials continues to attract the interest of the scientific community due to their fascinating properties and the plethora of promising applications in photovoltaic and optoelectronic devices. To enhance the efficiency and stability of perovskite-based devices, it is essential to discover novel compounds but also to investigate their various physicochemical, structural, and thermal properties. In this work, we report the synthesis and structural characterization of two novel hybrid lead bromide perovskites, combining the imidazolium cation (IMI) with methylammonium (MA) or formamidinium (FA) cations. The isolated polycrystalline powders were studied with X-ray powder diffraction (XPRD) and were formulated as (IMI)(MA)Pb_2Br_6, a 3D structure consisting of dimers of face-sharing octahedra linked in corner-sharing mode, and (IMI)(FA)$PbBr_4$, a 2D (110) oriented layer structure with zig-zag corner-sharing octahedra. The thermal stability of (IMI)(MA)Pb_2Br_6 and (IMI)(FA)$PbBr_4$ was investigated with thermogravimetric (TG) and differential scanning calorimetry (DSC) experiments which showed that both compounds are chemically stable (at least) up to 250 °C. Variable-temperature X-ray diffractometric (VT-XRD) studies of (IMI)(FA)$PbBr_4$ highlighted a structural modification occurring above 100 °C, that is a phase transformation from triclinic to orthorhombic, via an elusive monoclinic phase.

Keywords: lead halides; perovskites; imidazole; formamidinium; methylammonium; thermal analyses; powder diffraction

Citation: García-Espejo, G.; Konidaris, K.F.; Guagliardi, A.; Masciocchi, N. Using Imidazolium in the Construction of Hybrid 2D and 3D Lead Bromide Pseudoperovskites. *Chemistry* **2023**, *5*, 1329–1342. https://doi.org/10.3390/chemistry5020090

Academic Editor: Catherine Housecroft

Received: 27 April 2023
Revised: 24 May 2023
Accepted: 25 May 2023
Published: 26 May 2023

1. Introduction

Hybrid organic–inorganic halide perovskites represent an important area of research in the fields of chemistry, materials science and engineering, mainly due to their applications in photovoltaic technology of solar cells [1,2]. Owing to their inherent properties, perovskite solar cells display exceptional charge transport, dielectric constants and low exciton binding energy, allowing the construction of devices with power conversion efficiency (PCE) reaching up to 26% [3]. Apart from photovoltaics, metal-halide perovskites have also been proposed as an alternative scaffold for optoelectronic devices, such as light-emitting diodes (LEDs) [4–6] and photodetectors [7–9]. However, the actual performance and operational stability of these devices are highly dependent on the occurrence of thermally activated processes, such as phase transformations or material degradation [10]; therefore, studying the thermal behavior and stability ranges of metal halide perovskites is of paramount importance. Recently, it has been reported that the formation of 2D/3D hybrids, in which thin films of the pristine 3D perovskites are co-precipitated with a small amount of lower-dimensionality analogues, provides a significant improvement in the stabilization of perovskites, without being too detrimental to their photophysical performances [11–13]. Additionally, the family of metal-halide

perovskites shows great potential for thermoelectric generators [14]; in this case, the ultralow thermal conductivity of lead-halide perovskites may be advantageous [15,16], while for the vast majority of optoelectronic devices, heat transfer may be an issue and thermal management requires particular attention. It is well documented that the crystal structure of some of the most studied perovskites undergoes phase transformations slightly above room temperature. For example, at ~57 °C, the tetragonal phase of $MAPbI_3$ (MA = methylammonium) has been found to reversibly transform to cubic [17]. Solid-to-solid frequent phase transformations, whether of the reconstructive or of the displacive type, typically weaken the material stability, making the crystals, or grain, rather brittle, and increase the specific surface area, responsible for material degradation in environmental conditions. $MAPbI_3$ also displays high thermal expansion coefficients (κ_v = 157 MK^{-1}), with values surpassing those of many other semiconducting materials [18]. Both the crystalline phase and thermal expansion also influence electronic properties, such as carrier mobility, directionality and long carrier dynamics [19]. More severely, substantial decomposition effects for MA-based perovskites have been found to occur already below 100 °C even in an inert atmosphere [20], fostered by elimination of gaseous species, methylamine and HI. Consequently, heating without a lack of thermal management may be detrimental in various ways [21]. This holds particularly for solar cells and LEDs and the prospects of electrically or continuous wave-operated perovskite lasers [22].

Recently, we have investigated the thermal properties of lead iodides containing heterocyclic cations [imidazolium (IMI) and histammonium (HIST)] as the organic spacers. The synthesized compounds, imidazolium lead iodide, $(IMI)PbI_3$, and histammonium lead iodide, $(HIST)PbI_4$, demonstrated high thermal stability and ultralow thermal conductivity [23], a feature which was attributed to cation disorder, or lattice dynamics. Imidazolium cations have been widely employed as additives in perovskite solar cells to increase their stability [24], while they have also shown to play a role in the construction of materials with high thermal expansion resistance. For example, in the case of a single-crystal Cu(II) complex, the collective reorientation of IMI cations provokes a giant thermal expansion effect [25]. In lead bromides systems, Smółka et al. have recently reported the isolation of $(IMI)PbBr_3$, $(IMI)_2PbBr_4$, and $(IMI)_3PbBr_5$ structures, all of which exhibit solid–solid phase transitions upon increasing temperature [26], whereas Lightfoot and co-workers have reported the (110)-oriented two-dimensional hybrid $(IMI)(GU)PbBr_4$ perovskite (GU stands for guanidinium) [27]. Herein, we combined imidazolium cations with the commonly used methylammonium (MA) or formamidinium (FA) ones, and isolated two new compounds, the 3D $(IMI)(MA)Pb_2Br_6$ and the 2D $(IMI)(FA)PbBr_4$ species, respectively. These materials were characterized by X-ray powder diffraction (XRPD) methods, X-ray fluorescence (XRF) and diffuse-reflectance ultraviolet-visible (UV–Vis) spectroscopy. Thermogravimetric (TG), differential scanning calorimetry (DSC) and variable-temperature X-ray diffraction (VT-XRD) studies were carried out to assess their thermal stability and the occurrence of solid–solid phase transitions.

2. Materials and Methods

2.1. Materials

Lead oxide (PbO, >99.9%), imidazole (IMI, >95%), methylammonium chloride [(MA)Cl, >99%], formamidinium bromide [(FA)Br, >99%] and hydrobromic acid (HBr, 48% *w*/*w* in H_2O) were purchased from Merck KGaA (Darmstadt, Germany). All reagents were used as received without any further purification.

2.2. Syntheses

2.2.1. $(IMI)(MA)Pb_2Br_6$ (**1**)

PbO powder (2 mmol) was dissolved in 3 mL of HBr solution by stirring and heating the mixture up to 70 °C. Subsequent addition of (MA)Cl powder (1 mmol) caused the immediate precipitation of an orange solid, $(MA)PbBr_3$. The precipitate was redissolved under vigorous stirring and heating the solution up to ca. 150 °C.

Next, IMI powder (4 mmol) was added to the mixture, being dissolved quickly. Then, stirring was discontinued, and the solution was left to slowly cool down up to 90 °C, keeping fixed this temperature for 3 h, during which time a creamy white precipitate started to crystallize. Finally, with the solution still at 90 °C, the polycrystalline material was collected and dried by filtration under vacuum. Left in air at room temperature overnight, the material formulated as (IMI)(MA)Pb_2Br_6 turned orange and was proved, by X-ray diffraction methods, to be a single polycrystalline phase (see Figure S1).

2.2.2. (IMI)(FA)$PbBr_4$ (**2**)

Method A: PbO powder (1 mmol) was dissolved in 2 mL of HBr solution by stirring and heating the mixture up to 70 °C. Subsequent addition of (FA)Br powder (1 mmol) caused the immediate precipitation of an orange solid, (FA)$PbBr_3$. The precipitate was redissolved under vigorous stirring and heating the solution up to ca. 120 °C. Next, IMI powder (3 mmol) was added to the mixture, being dissolved quickly. Then, stirring was discontinued and the solution was left to slowly cool down to room temperature overnight, during which time a creamy white precipitate started to crystallize (see Figure S1). Finally, the polycrystalline material formulated as (IMI)(FA)$PbBr_4$ was collected and dried by filtration under vacuum. Method B: PbO powder (1 mmol) was dissolved in 4 mL of HBr solution by stirring and heating the mixture up to 70 °C. Subsequent addition of (FA)Br powder (1 mmol) caused the immediate precipitation of an orange solid, (FA)$PbBr_3$, which was redissolved by stirring and heating the solution up to 70 °C. The resulting solution was left to slowly cool down at room temperature overnight, but no precipitation occurred. The next day it was layered with Et_2O (1:1) and a powder containing tiny needles was obtained after the two layers mixed (see Figure S1). The powders were then collected by filtration, washed with Et_2O and dried under vacuum.

2.3. Characterization

2.3.1. X-ray Powder Diffraction (XRPD) Structural Analysis

Powders of (IMI)(MA)Pb_2Br_6 and (IMI)(FA)$PbBr_4$ were deposited in the hollow of a 0.2 mm deep silicon monocrystal (a zero background plate, supplied by Assing spa, Monterotondo, Italy). Minimization of evident textural effects for (IMI)(FA)$PbBr_4$ was achieved by mixing the powder with 10% *w*/*w* amorphous Cabosil® (Sigma-Aldrich). It also proved difficult to grind this material because it immediately degraded, giving very broad diffraction peaks (see Figure S2). Diffraction data were collected in the 5–105° 2θ range, on a D8 Bruker AXS vertical sampling diffractometer, operating in θ:θ mode equipped with a linear Lynxeye position sensitive detector, set at 300 mm from the sample (generator settings: 40 kV, 40 mA, Ni-filtered Cu-K$\alpha_{1,2}$ radiation, λ_{avg} = 1.5418 Å). XRPD data for structure solution were collected at the 3–105° 2θ range for both materials, sampling at 0.02°, with scan time lasting ca. 16 h.

Peak search and profile fitting allowed the location of the most prominent, low-angle peaks, which were later used in the indexing process by the TOPAS-R software [28]. Approximate lattice parameters of primitive cells were determined to be $a = b = 9.09$, $c = 13.88$ Å, $\alpha = \beta = 90°$ and $\gamma = 120°$ [GOF(20) = 354.7] and $a = 10.78$, $b = 9.09$, $c = 21.51$ Å, $\alpha = 45.9$, $\beta = 32.4$ and $\gamma = 34.6°$ [GOF(20) = 21.9] (later reduced by the LePage algorithm [29]) for (IMI)(MA)Pb_2Br_6 and (IMI)(FA)$PbBr_4$, respectively. Lattice symmetry and systematic absences conditions suggested $P6_3/mmc$ [(IMI)(MA)Pb_2Br_6] and $P\bar{1}$ [(IMI)(FA)$PbBr_4$] as plausible space groups, later confirmed by successful structure solution and refinement. Real space structure modelling by the simulated annealing algorithm coupled to Monte Carlo-search allowed the definition of suitable models, initially defined by freely floating Pb and Br atoms and subsequently improved through the addition of IMI, MA and FA cations as rigid bodies of known (and rigid) geometry. The most satisfactory model was then later refined by the Rietveld method. Both structure solution and final refinements were carried out by TOPAS-R software. The background contribution was modelled by a Chebyshev polynomial fit; atomic scattering factors for

neutral atoms were taken from the internal library of TOPAS-R. Preferred orientation corrections, in the March–Dollase formulation [30] was applied for (IMI)(FA)$PbBr_4$ on the [001] pole (with final magnitude g_{001} = 0.850(3)), while a spherical harmonics approach has been employed for ((IMI)(MA)Pb_2Br_6), leading, in both cases, to significantly lower agreement factors. Crystal data and relevant data analysis parameters are collected in Table 1. Figure 1 shows the final Rietveld refinement plots. Fractional atomic coordinates have been deposited as CIF files within the Cambridge Crystallographic Database as publications No. CCDC 2259136-2259137.

Table 1. Crystal data and refinement parameters for (IMI)(MA)$PbBr_4$ (**1**), (IMI)(FA)$PbBr_4$ (**2**) and (IMI)(GU)$PbBr_4$.

Parameter	**(IMI)(MA)Pb_2Br_6**	**(IMI)(FA)$PbBr_4$**	**(IMI)(GU)$PbBr_4$ [27]**
Chemical formula	$C_4H_{11}Br_6N_3Pb_2$	$C_4H_{10}Br_4N_4Pb$	$C_4H_{11}Br_4N_5Pb$
Fw, amu	994.97	640.96	656.01
Crystal system	Hexagonal	Triclinic	Triclinic
Space group	$P6_3/mmc$	P-1	P-1
a (Å)	9.0885(1)	6.0996(4)	6.1106(4)
b (Å)	=*a*	9.0669(8)	9.2753(5)
c (Å)	13.8787(1)	13.1358(8)	13.0429(9)
α (°)	90	92.931(3)	93.474(9)
β (°)	90	92.212(4)	92.726(9)
γ (°)	120	91.885(6)	91.258(8)
V (Å^3)	992.80(2)	724.53(9)	736.82(8)
Z	2	2	2
Molar volume, *V*/*Z* (Å^3)	496.40	362.26	368.41
T (K)	293	293	298
λ, (Å)	Cu-Kα_{12}, 1.5418	Cu-Kα_{12}, 1.5418	Mo-Kα_{12}, 0.71075
Method	Powder X-ray diffraction	Powder X-ray diffraction	Single crystal X-ray diffraction
μ (mm^{-1})	45.6	34.69	22.27
ρ_{calc} (g cm^{-3})	3.320	2.938	2.957
2θ—range (°)	10–105	6–105	5.5–50
R_p, R_{wp}	0.066–0.092	0.050–0.067	n.a.
R_{Bragg}	0.089	0.040	0.065

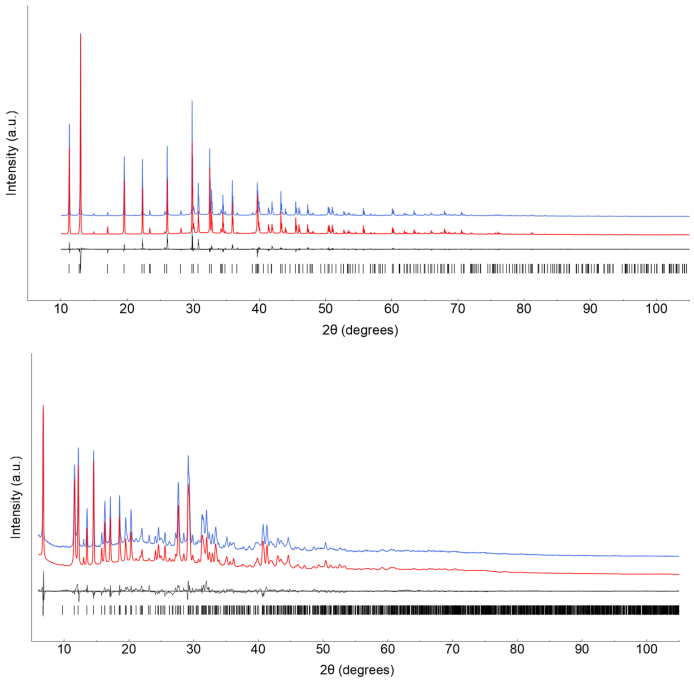

Figure 1. Rietveld refinement plots for (IMI)(MA)Pb_2Br_6 (**1**, **top**) and (IMI)(FA)$PbBr_4$ (**2**, **bottom**). Observed data in blue (slightly offset for clarity), calculated trace in red, difference plot in grey and tick markers for peak positions in black. Drawn with Gnuplot [31].

2.3.2. X-ray Fluorescence Measurements

Gently ground powders of the crystalline RT-phases were deposited on a polycarbonate film and analyzed with a MiniPal2 XRF spectrometer (PANalytical B.V., Almelo, The Netherlands), equipped with a Cr-anode operating at 30 kV and 2 μA. X-ray fluorescence lines were measured for Pb (L_α and L_β lines, at 10.5 and 12.6 keV, respectively) and Br (K_α and K_β lines, at 11.9 and 13.3 keV, respectively). Using a reference $PbBr_2$ powder (100% pure crystal phase, XRPD evidence), XRF peak integration and normalization enabled the experimental evaluation of the Pb:Br ratio, found to be 1:3 and 1:3.9 in (IMI)(MA)Pb_2Br_6 and (IMI)(FA)$PbBr_4$, respectively.

2.3.3. Diffuse Reflectance UV–Vis Spectroscopy

UV–Vis–NIR reflectance spectra of the powders were measured in the 200–900 nm range using a UV-2600 Shimadzu spectrometer. $BaSO_4$ was used as a non-absorbing reflectance reference. The Kubelka–Munk function F[R] was calculated from the reflectance spectrum, using the $F[R] = (1 - R)^2/2R$ relationship. Taking F[R] as the representative of the sample absorbance spectrum, extrapolation of the linear portion of the $(F[R]\ h\nu)^2$ vs. $h\nu$ plot on the $h\nu$ axis provided experimentally accessible direct band gap values (Tauc plots) [32].

2.3.4. Thermal Characterization

Thermogravimetric (TG) and differential scanning calorimetry (DSC) traces were acquired from 30 to 400 °C (with a scan rate of 10 °C min^{-1}) using a Netzsch STA 409 PC Luxx® analyzer under a N_2 flow and with alumina sample holders equipped with a pierced lid.

Variable temperature (VT-XRPD) experiments were performed from 30 to 300 °C to assess thermal and polymorphic stability. Powdered batches were deposited in the hollow of an aluminum sample holder of a custom-made heating stage (Officina Elettrotecnica di Tenno, Ponte Arche, Italy). Diffractograms were acquired in air, in the most significant (low-angle) 2θ range, under isothermal conditions in 20 °C steps.

3. Results and Discussion

3.1. Synthetic Comments

Compounds (IMI)(MA)Pb_2Br_6 (**1**) and (IMI)(FA)$PbBr_4$ (**2**) were synthesized by adding lead(II) oxide, imidazole (in its neutral form) and methylammonium or formamidinium halide salts in a hot HBr solution, following the steps detailed in the Section 2.2. Syntheses. It is worth to note that the halides contained in the ammonium-derived salts used as precursors are irrelevant since the HX acid acting as solvent is in excess and, therefore, will define the halide found in the structure of the resulting product. The global reactions of the synthetic processes (1) and (2), where imidazole is transformed to the positively charged species imidazolium (IMI), are shown hereafter.

$$2PbO + (MA)Cl + 6HBr + C_3H_4N_2 \rightarrow (IMI)(MA)Pb_2Br_6 + 2H_2O + HCl \quad (1)$$

$$PbO + (FA)Br + 3HBr + C_3H_4N_2 \rightarrow (IMI)(FA)PbBr_4 + H_2O \quad (2)$$

To avoid the precipitation of both starting materials and intermediates and to ensure the isolation of pure compound **1**, its crystalline powder was filtrated at high temperature (Section 2.2. Syntheses). In addition, when the synthesis of **1** was undertook by mixing the starting reagents in stoichiometric ratio, the orange (MA)$PbBr_3$ phase was identified in the precipitate instead. Surprisingly, only when a 2:1:4 ratio was employed among PbO/(MA)Cl/imidazole precursors, (IMI)(MA)Pb_2Br_6 crystals were clearly found without contamination of side phases. The use of an excess of imidazole may force in some extent the precipitation of **1** instead of the, apparently, more stable (MA)$PbBr_3$ perovskite. Finally, several trials were also performed with the aim to obtain alternative species that share the architecture of **1** or **2** but slightly different chemical composition. In one hand, when the

substitution of bromide with iodide was attempted, (IMI)PbI_3 compound was permanently found, regardless of the cation employed to accompany IMI. On the other hand, when Cs^+ was used together with IMI in HBr syntheses, the resulting species was $CsPb_2Br_5$ [33].

3.2. Comparative Crystal Structure Analysis

(IMI)(MA)Pb_2Br_6 (**1**) crystallizes in the hexagonal space group, $P6_3/mmc$. The structure contains octahedrally coordinated Pb^{2+} ions lying on a 3 m. special positions (at 1/3, 2/3, z, Wyckoff f), surrounded by six Br^- anions, three of the Br1 type (on inversion centers of the .2/m. type, Wyckoff g) and three on a mirror plane normal to *c* (at x, 2x, 1/4, mm2 symmetry, Wyckoff h). Overall, the inorganic framework is three-dimensional. Imidazolium (IMI) and methylammonium (MA) cations occupy different cavities in the crystal structure of **1**, of markedly different size and shape. IMI lies on a crystallographic site of −3 m. symmetry, incompatible with its "ideal" discoidal D_{5h} symmetry, and, therefore, was modeled with a heavily disordered fragment with site occupancy factors (sof's) of 1/12; similarly, though to a lesser extent, also MA was found disordered, with C/N atoms sharing the same crystallographic site (1/3, 2/3, z, Wyckoff f) across a crystallographic mirror plane. Figure 2 depicts the local geometry of the Pb/Br framework; Figure 3a,b illustrate the overall crystal packing (viewed down *a* and *c*, respectively), with the highly disordered (perhaps rattling) IMI cations represented as pink spheres and the MA cations rigidly encapsulated in the crystal structure through weak (here, equivalent) C/NH···Br "intermolecular" interactions (C/N ··· Br distance of ca. 3.80 Å). Interestingly, the dynamic disorder of IMI (and other) cations in low-dimensional perovskitoid phases has been considered a valuable feature enormously decreasing thermal conductivity for thermoelectric applications [23]. Finally, in such a complex space group symmetry, the reader is warmly asked to use the supplied cif file for a better rendering.

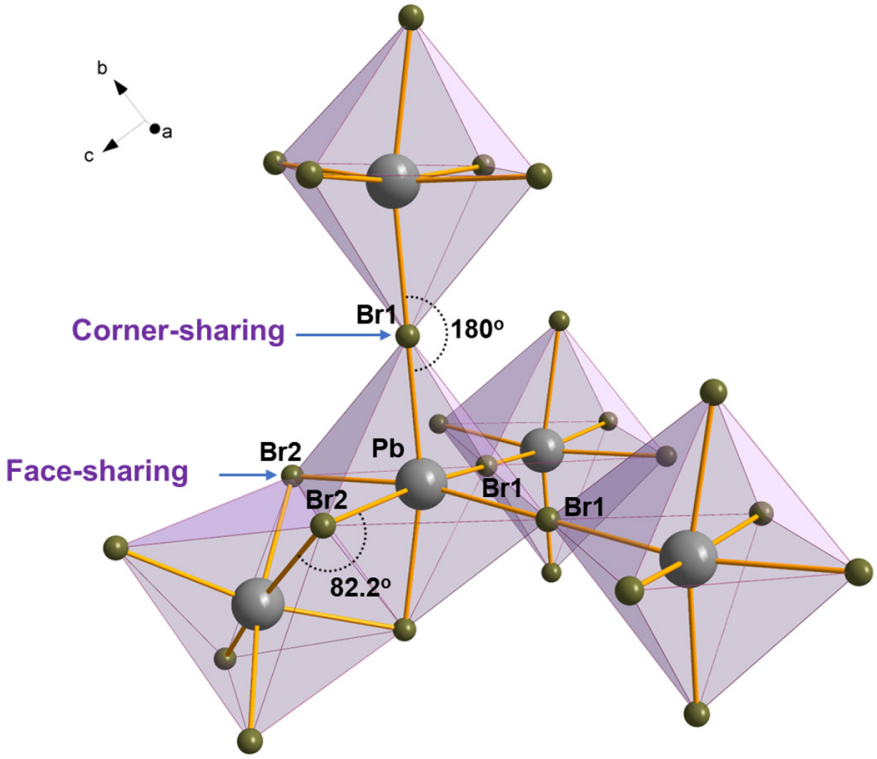

Figure 2. The coordination environment of a Pb^{2+} cation, showing how different coordination geometries of the Br^- ligands lead the formation of both corner-sharing and face-sharing octahedra. Only the Br^- ligands of the central Pb^{2+} are labelled.

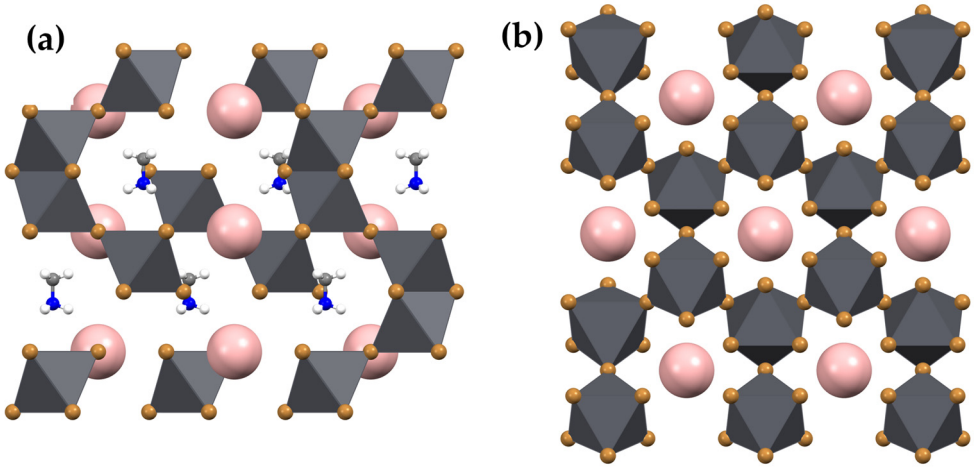

Figure 3. Views down the crystallographic *a* (**a**) and *c* (**b**) axes of the crystal structure of (IMI)(MA)Pb_2Br_6 (**1**). Heavily disordered IMI cations are drawn as pink (featureless) spheres.

In **1,** the $[PbBr_6]^{4-}$ octahedra display two different connectivities: indeed, pairs of face-sharing octahedra (connected by the Br2 ions), with their threefold axis aligned with *c*, are mutually linked, through a single bromine atom (here, Br1), in a corner-sharing manner. This is schematically shown in Figure 2, whereas the chemically relevant geometrical parameters are synoptically collected in Table 2. Such differentiation of Br ions is easily understood: (i) three μ_2-Br1 atoms form Pb-Br1 bonds (of 3.000(1) Å distance) and a complete linear (180°) Pb-Br1-Pb angle, while (ii) the other three (bent) μ_2-Br2 ligands form Pb-Br2 bonds of 3.040(3) Å distance and a Pb-Br2-Pb angle of 83.1(1)°. Cis-Br-Pb-Br angles lie in the 80.8(1)–96.5(1)° range, while the unique trans Br-Pb-Br angle amounts to 167.44(8)°. Intradimer and interdimer non-bonding interactions of the Pb ... Pb type are 4.03 and 6.00 Å, respectively. The latter is slightly longer than the Pb ... Pb (cell edge) of the high-temperature $CsPbBr_3$ cubic polymorph (ca. 5.873 Å at 473 K), which shares the same face-sharing motifs with linear Pb-Br-Pb links [34], manifesting the non-innocent (inflating) nature of the large cation(s). Since all dimers can be idealized as $[Pb_2Br_3]^+$ nodes mutually linked by 6 shared Br1 ions, one may question whether this framework could be idealized as a $[Pb_2Br_3]^+[Br]_{6/2}$ perovskitic one (i.e., $[Pb_2Br_6]^{2-}$ being topologically equivalent to $[PbBr_{6/2}]^-$). However, since $[Pb_2Br_6]^{2-}$ (and its connected Br1 atoms) may be ideally reduced to a trigonal prism of D_{3h} symmetry with eclipsed Pb-Br1 bonds, whereas $[PbBr_{6/2}]^-$ shows a fully staggered conformation of O_h symmetry, this is not the case, and the two framework are topologically different. The coexistence of corner-sharing and face-sharing octahedra is not unprecedented in perovskite chemistry as it has been previously reported by the group of Kanatzidis et al. on germanium [35] and tin [36] iodide perovskites.

(IMI)(FA)$PbBr_4$ (**2**) crystallizes in the triclinic space group, $P\bar{1}$. Its crystal structure contains octahedral $[PbBr_6]^{2-}$ anions sharing four μ_2-bridging Br^- ligands with neighboring Pb^{2+} ions and possessing two Br ions as monodentate (terminal) ligands, in *cis* position one to the other. All atoms (but two: Br2 and Br5, which lie on different inversion centers—Wyckoff *c* and *a*, respectively) are in general position (Wyckoff *i*). The inorganic portion, of 2D character, thus adopts a zig-zag arrangement of corner-sharing octahedra (depicted in Figure 4), running infinitely in the *ab* plane, and stacked (and separated) along *c* by the presence, in different cavities, of the IMI and FA cations. This sequence of octahedral is reminiscent of a very thin (110) cut of the archetypal 3D perovskite network [37]. In **2** the terminal bromines are marginally, but systematically, closer to the Pb^{2+} ions to which they are directly linked (Pb-Br 2.88(1) and 2.96(1) Å) than the bridging ones (3.014(17)–3.196(6) Å). The shortest non-bonding interactions of the Pb ... Pb type fall in the 6.10–6.39 Å range and are even more (positively) strained than in **1**.

Table 2. Relevant geometrical features for (IMI)(MA)$PbBr_4$ (**1**), (IMI)(FA)$PbBr_4$ (**2**) and (IMI)(GA)$PbBr_4$, synoptically collected.

Parameter	(IMI)(MA)Pb_2Br_6	(IMI)(FA)$PbBr_4$	(IMI)(GA)$PbBr_4$ [27]
Pb ··· Pb (Å)	4.03; 6.00	6.10–6.39	6.06–6.23
Pb-Br (Å)	3.000(1)–3.040(1)	2.88(1); 2.96(1) **t** 3.014(17)–3.196(6) **b**	2.911(2); 2.933(2) **t** 3.036(2)–3.140(1) **b**
cis-Br-Pb-Br (°)	80.8(1)–96.5(1)	84.0(3)–95.9(4)	86.01(4)–95.19(2)
trans-Br-Pb-Br (°)	167.44(8)	169.0(4)–178.4(3)	171.1–175.9
Pb-Br-Pb (°)	83.1(1)–180	169.0(4)–180	178.08(7)–180
Topology	Dimers of face-sharing octahedra mutually linked in corner-sharing mode	Corrugated 2D layers from (110)-cuts of 3D perovskite	Corrugated 2D layers from (110)-cuts of 3D perovskite
IMI cation	Heavily disordered	Ordered	Ordered
MA or FA cation	C/N disorder	"Ordered" (see text)	Disordered
Optical band gap (eV)	3.08	2.88	2.94

t = terminal; **b** = bridging.

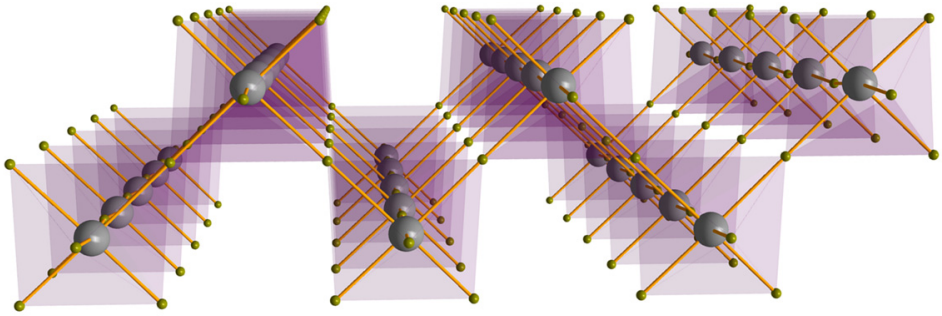

Figure 4. The zig-zag (ladder-like) arrangement of the corner-sharing $[PbBr_6]^{4-}$ octahedra in the crystal structure of the (IMI)(FA)$PbBr_4$ (**2**).

A view down the crystallographic *a* axis of compound **2**, portrayed in Figure 5, shows how the arrangement of the $[PbBr_6]$ octahedra allows the encapsulation of imidazolium and formamidinium cations in different cavities. In more detail, the zig-zag (corner sharing) arrangement of the $[PbBr_6]$ octahedra leaves free cavities for the FA cations, which, accordingly, position themselves as much as they do in the pristine 3D $FAPbBr_3$ system [38], though no disorder of the FA cation was here modeled. At variance, the IMI cations are segregated in parallel layers sandwiched between two inorganic slabs. This arrangement was also found in the isostructural guanidinium (GU) system, of (IMI)(GU)$PbBr_4$ formulation [27], the relevant structural features of which are added, for comparison, in both Tables 1 and 2. Thus, an alternative (structure-based) formulation for the two (IMI)(CAT)$PbBr_4$ (CAT = FA, GU) systems could be well presented as [IMI][(CAT)$PbBr_4$], with IMI and [(CAT)$PbBr_4$] layers (positively and negatively charged, respectively) alternating along *c* in an ... ABAB ... sequence.

As an interesting caveat of the structural chemistry of these species, it is worth mentioning that the ionic radii of MA, FA, GU and congeners, computed by a number of methods and reaching a general consensus (see Table 1 in ref. [11]), are not enough to predict the structure and topology of mixed-cations perovskitoids. Indeed, MA and FA possess similar (and small) ionic radii (below 250 pm), and can tuck in the cavities, or pockets, of 3D or (110) layered perovskites. Differently, cations with ionic radii above 250 pm (IMI, azetidinium and larger ones) find their location outside these layers. Why GU (ionic radius of ca. 270 pm) can snug fit into the perovskite pockets must then be a consequence of the weak(er), but significant, H-bond interactions with the inorganic framework, justified not only by size, but also by shape and, ultimately, by subtle energetic stabilization, including non-negligible entropic effects for disordered (and dynamic) systems.

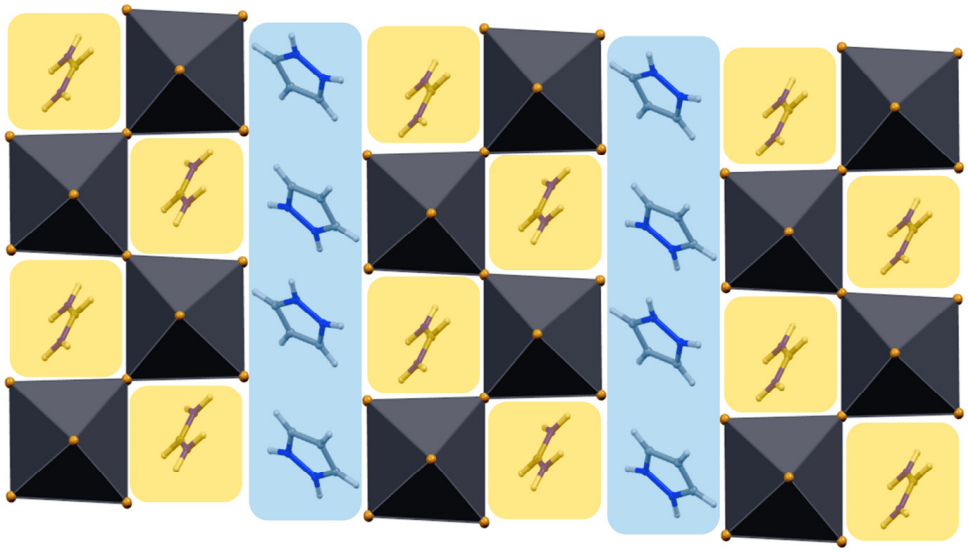

Figure 5. View down the crystallographic *a* axis for (IMI)(FA)$PbBr_4$ (**2**). The formed cavities are emphasized with different colors for imidazolium (blue) and formamidinium (yellow) cations.

3.3. UV–Vis Diffuse Reflectance Measurements

Powders of (IMI)(MA)Pb_2Br_6 and (IMI)(FA)$PbBr_4$ appear orange and creamy white, respectively, at the naked eye level and, therefore, they are expected to possess semiconducting optical band gaps (E_g) at high enough energies, close to the UV type A photon energy regime. The use of the full reflectance spectra (R), collected in the 200–900 cm^{-1} range (UV to near infrared regime), the Kubelka–Munk pseudo-absorption spectra (F[R]) and their transformation to $(F[R]h\nu)^2$ for a direct allowed transition (Tauc plot), enabled the determination, of E_g values, found to be 3.08 and 3.07 eV for **1** and **2**, respectively. Figure 6 shows the relevant plots mentioned above. As these values refer to experimentally detectable (symmetry allowed) transitions, they can be interpreted as an upper limit estimate of the frontier-orbital separation, which, therefore, must be lower than (or equal to) 3.07 eV. The nearly colorless aspect of (IMI)(FA)$PbBr_4$ is in line with the strong confinement of excitons determined by quantum effects in single-layer (though corrugated) of [$PbBr_4$] slabs, excised from a (110) surface of a 3D perovskite (as also manifested in (IMI)(GU)$PbBr_4$, which shows an E_g value of 2.94 eV [27]). More surprising is the high optical band gap energy value observed in the (IMI)(MA)Pb_2Br_6 3D system, which, though topologically different from the 3D archetype, shares the same "ideal" formulation (ABX_3) and the corner-sharing octahedra structure. Apparently, the presence of face-sharing dimers in the 3D network is highly detrimental to charge delocalization, acting as impassable barriers for electrons and holes diffusion.

3.4. Thermal Stability Measurements

Thermogravimetric and DSC analyses of (IMI)(MA)Pb_2Br_6 (shown in Figure 7a) indicate that this crystal phase is stable up to ca. 270 °C, where an inflection point of the TG curve, possibly due to incipient decomposition and methylamine/HBr release, is observed. In the pristine $MAPbBr_3$ phase (slightly more stable than the nowadays ubiquitous $MAPbI_3$ one [39]), the decomposition temperature is reported to be ca. 340 °C (from Differential Thermal Analysis) [40]. Because of the relatively unstable nature of MA-containing phases, we collected XRPD data on a sample kept in environmental conditions for six weeks and did not observe any significant change (see Figure S3).

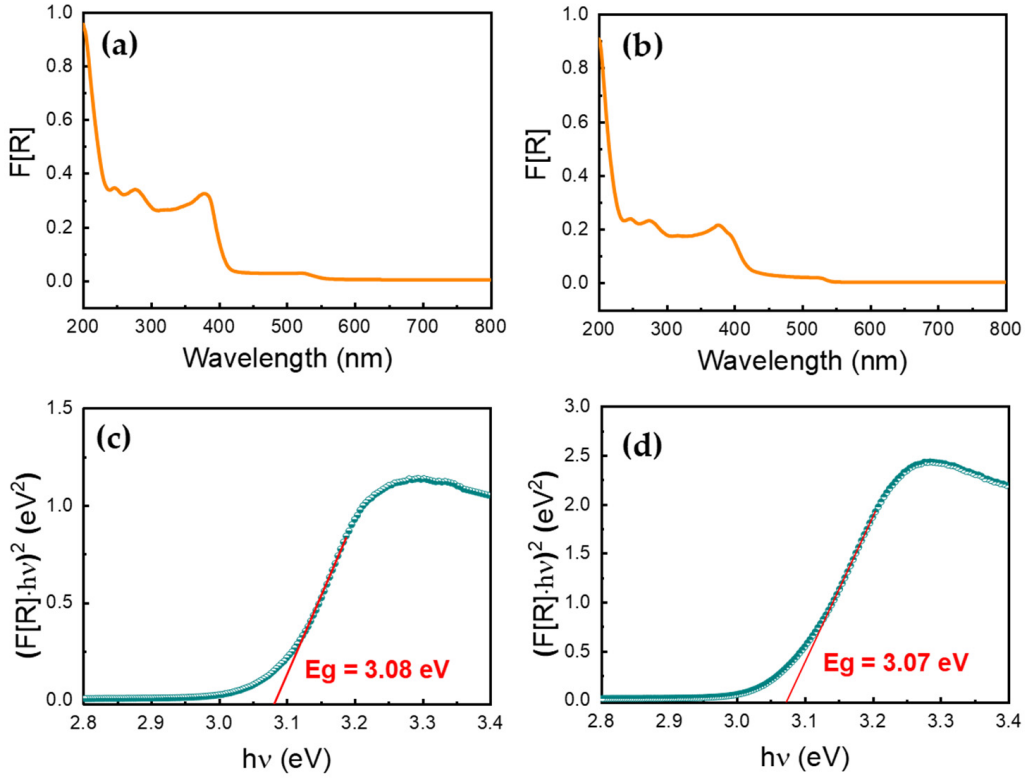

Figure 6. The Kubelka–Munk spectra for compounds **1** (**a**) and **2** (**b**), and their corresponding Tauc plots for **1** (**c**) and **2** (**d**).

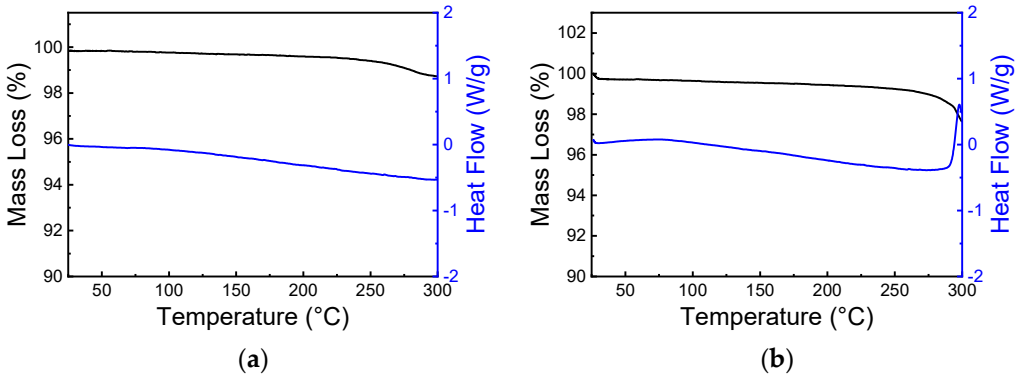

Figure 7. Thermogravimetric (black) and differential scanning calorimetric (blue) curves for (IMI)(MA)Pb_2Br_6 (**1**) (**a**) and (IMI)(FA)$PbBr_4$ (**2**) (**b**) phases.

Variable temperature X-ray diffraction was used to follow the thermal stability and evolution of the different crystal phases. The raw data are plotted in Figures S4 and S5. Substantial stability of (IMI)(MA)Pb_2Br_6 (**1**) phase is demonstrated in a wide temperature range, from room temperature to (at least) 250 °C (see Figure 8a), with no changes of the diffraction pattern, apart from expected thermally-induced lattice strain. Thermal expansion coefficients, derived from the analysis of the trend of the relative changes of the *a* and *b* axes lengths and the cell volume vs. temperature (Figure 8c), are: κ_a = 10.3, κ_c = 81.0 and κ_V = 102 MK^{-1} (for $p = p_0$ (1 + κ_p(T − T_0)); *p* = *a*, *c* and *V*). The estimated values are in line with those observed in similar species [23] and demonstrate a substantial flexibility of the crystal lattice. The inset of Figure 8c shows the thermal strain tensor, determined by Ohashi's method [41] and graphically represented by the Wintensor software [42].

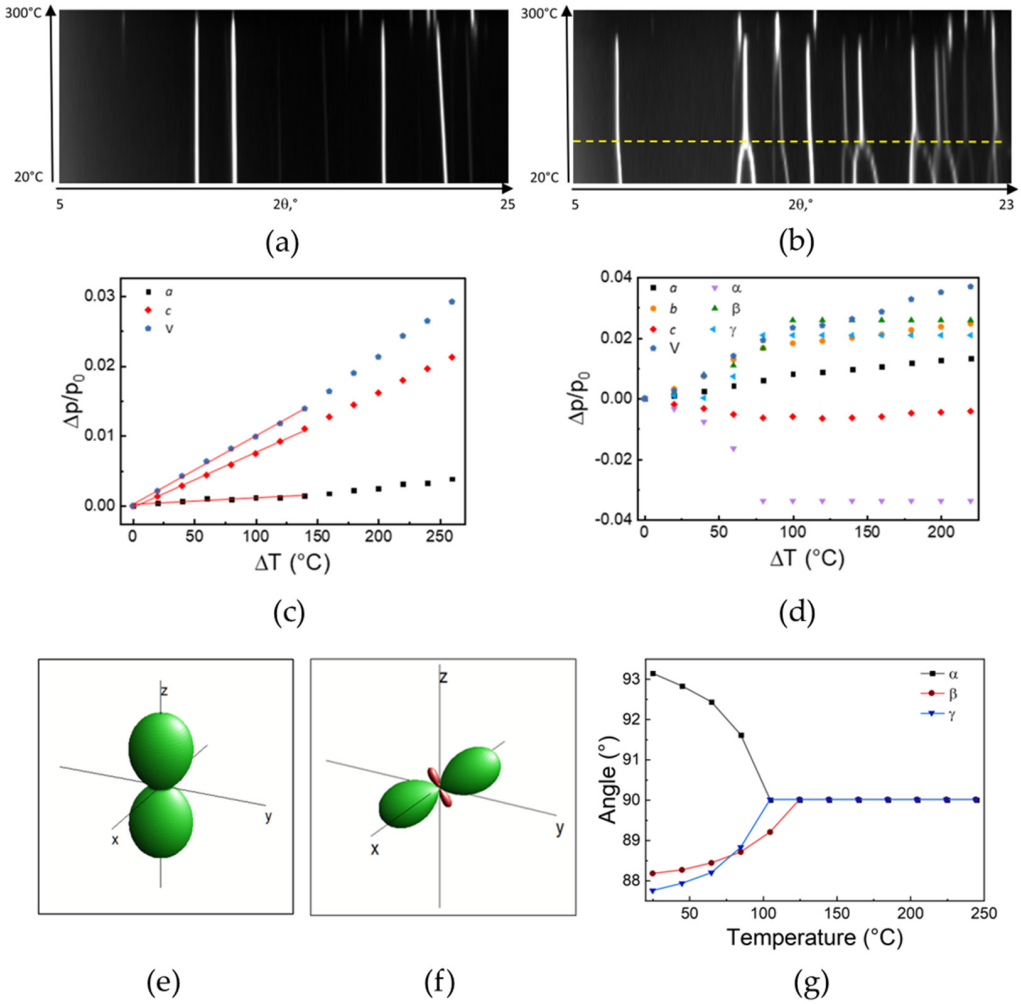

Figure 8. The thermal evolution, with increasing temperature, of both the XRPD patterns and the lattice parameters derived therefrom, expressed as $\Delta p/p_0$, and the visualization of the corresponding strain tensor for (IMI)(MA)Pb_2Br_6 (**1**) (**a**,**c**,**e**) and (IMI)(FA)$PbBr_4$ (**2**) (**b**,**d**,**f**). Slightly below 300 °C, decomposition of the two phases, occurs. In (**b**), the yellow dashed line indicates the occurrence of a solid–solid phase change. In (**g**), lattice angles evolution (°) vs. temperature (°C) for (IMI)(FA)$PbBr_4$ (**2**), showing the progressive transformation from the triclinic to orthorhombic symmetry, through an elusive monoclinic phase (β < 90° at 100 °C).

The same kind of thermal characterization was also performed on (IMI)(FA)$PbBr_4$ (**2**), which proved to behave in a rather different manner. Although thermal stability was still high (no decomposition being observed below 250 °C), Figure 7b shows a broad bump in the 70–100 °C range, the nature of which could only be explained by analyzing (and visualizing) VT-XRD data (see Figure 8b). Here, a clear complex change of the diffraction peak position occurs upon raising the temperature, with several couples of peaks merging at about 100 °C into a single one. The evaluation of the lattice parameters showed that the three oblique angles, deviating from 90° as much as 2.9°, progressively change, in a continuous manner, to 90°, through an elusive monoclinic phase, and eventually landing into a fully orthorhombic polymorph. These changes are graphically illustrated in Figure 8f. The structural change is of the displacive type and can be easily understood by the sketches shown in Figure 9a,b (for the triclinic and orthorhombic polymorphs, respectively). Setting the interaxial angles to 90°, with very little shifts of the Pb and Br atoms, the Pmmb space group is obtained, which requires also a small reorientation of the IMI and FA cations, if not their partial disordering.

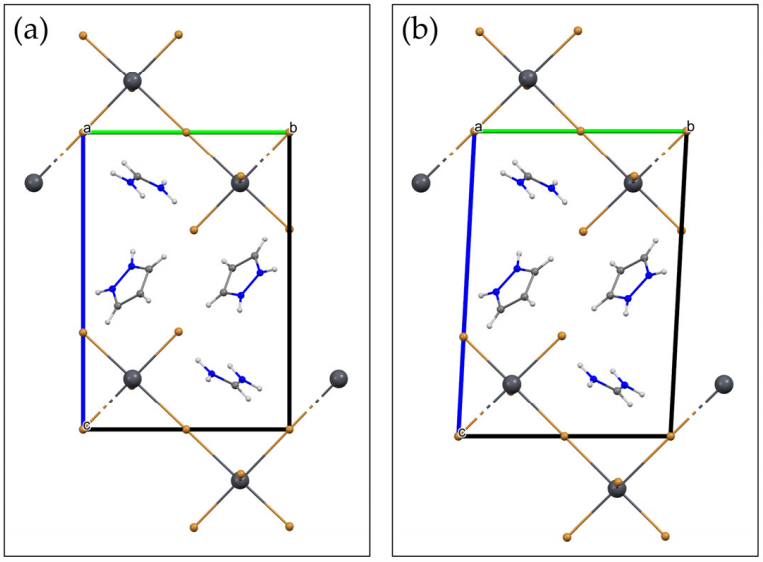

Figure 9. The structural change in (IMI)(FA)$PbBr_4$ (**2**) brought about heating. Views down ***a*** axis of the triclinic (**b**) and orthorhombic (**a**) polymorphs, mutually related by a displacive phase transition. The orientation of the IMI and FA cations in the latter is just a guide to the eye and does not conform to the Pmmb space group symmetry.

4. Conclusions

In this contribution, we describe the synthesis, structural and thermal characterization of two novel compounds, (IMI)(MA)Pb_2Br_6 (**1**) and (IMI)(FA)$PbBr_4$ (**2**), which join a handful of imidazolium lead(II) halides reported in the literature. Their crystal structures comprise two types of organic cations, imidazolium and a smaller one: methylammonium or formamidinium, respectively. The dimensionality of the structures was found to be dependent on the connectivity among the [$PbBr_6$] octahedra. In **1**, dimers of face-sharing octahedra connect with corner-sharing ones, allowing the structure to expand along all three dimensions (3D network), while in **2**, the [$PbBr_6$] units are linked via sharing corners, giving rise to 2D corrugated sheets. Interestingly, the zig-zag arrangement of the [$PbBr_6$] octahedra observed in **2** allows the formation of free cavities which host the formamidinium cations, while the imidazolium ones are found to form parallel layers sandwiched between two inorganic slabs. DSC and TGA measurements show that **1** and **2** are stable up to at least 250 °C, whereas VT-XRD studies on crystalline powders shed light on the polymorphic stability of the two crystal phases. (IMI)(MA)Pb_2Br_6 demonstrates a substantial flexibility of its crystal lattice reflected by a relatively high thermal κ_V coefficient of 102 MK^{-1}. On the other hand, the diffraction pattern of (IMI)(FA)$PbBr_4$ displays a critical change of peaks above 100 °C, resulting in a clear phase transition from the initial triclinic to a final orthorhombic polymorph. This paper evokes the study of alternative hybrid imidazolium-based systems, with the aim to investigate the influence of the metal (e.g., bismuth instead of lead) on their thermal behavior. Work can also be anticipated in the direction of adding other "prone to disorder" organic cations in search for low thermal conductivity species for thermoelectric applications.

Supplementary Materials: The following supporting information can be downloaded at: https://www.mdpi.com/article/10.3390/chemistry5020090/s1, Figure S1: Optical images of the prepared samples; Figure S2: XRPD pattern of pristine (blue) and gently ground (red) (IMI)(FA)$PbBr_4$ (**2**) showing partial and anisotropic degradation of the crystals; Figure S3: XRPD measurements of a powder sample of (IMI)(MA)Pb_2Br_6 (**1**) exposed to environmental air, humidity and light, in the course of 6 weeks. Figure S4: VT-XRD patterns for (IMI)(MA)Pb_2Br_6 (**1**) in the 25–345 °C range; Figure S5: VT-XRD patterns for (IMI)(FA)$PbBr_4$ (**2**) in the 25–345 °C range; CCDC Codes: 2259136-2259137.

Author Contributions: Conceptualization, N.M. and A.G.; investigation, G.G.-E. and K.F.K.; writing—original draft preparation, K.F.K. and N.M.; writing—review and editing, G.G.-E. and A.G.; supervision, N.M.; funding acquisition, A.G. and N.M. All authors have read and agreed to the published version of the manuscript.

Funding: The authors thank the Italian Ministry of Research for partial funding (Project PRIN 2017L8WW48, HY-TEC. Hybrid ThermoElectric Composites: Proof of concept for low-T, n-type and flexible thermoelectrics) and the University of Insubria for postdoctoral funding granted to G.G.-E. and K.F.K.

Data Availability Statement: The data presented in this study are available in the supplementary information or upon request to the corresponding authors. Crystal data and fractional atomic coordinates have been deposited at the Cambridge Crystallographic Data Center, CCDC Codes: 2259136-2259137. These data can be obtained free of charge via www.ccdc.cam.ac.uk/data_request/cif, by e-mailing data_request@ccdc.cam.ac.uk, or by contacting The Cambridge Crystallographic Data Centre, 12, Union Road, Cambridge CB2 1EZ, UK; fax: +44-1223-336033.

Conflicts of Interest: The authors declare no conflict of interest.

References

1. Jena, A.K.; Kulkarni, A.; Miyasaka, T. Halide Perovskite Photovoltaics: Background, Status, and Future Prospects. *Chem. Rev.* **2019**, *119*, 3036–3103. [CrossRef] [PubMed]
2. Zhang, W.; Wu, X.; Zhou, J.; Han, B.; Liu, X.; Zhang, Y.; Zhou, H. Pseudohalide-Assisted Growth of Oriented Large Grains for High-Performance and Stable 2D Perovskite Solar Cells. *ACS Energy Lett.* **2022**, *7*, 1842–1849. [CrossRef]
3. Park, J.; Kim, J.; Yun, H.-S.; Paik, M.J.; Noh, E.; Mun, H.J.; Kim, M.G.; Shin, T.J.; Seok, S.I. Controlled growth of perovskite layers with volatile alkylammonium chlorides. *Nature* **2023**, *616*, 724–730. [CrossRef] [PubMed]
4. Liu, X.-K.; Xu, W.; Bai, S.; Jin, Y.; Wang, J.; Friend, R.H.; Gao, F. Metal halide perovskites for light-emitting diodes. *Nat. Mater.* **2021**, *20*, 10–21. [CrossRef]
5. Yuan, S.; Wang, Z.-K.; Xiao, L.-X.; Zhang, C.-F.; Yang, S.-Y.; Chen, B.-B.; Ge, H.-T.; Tian, Q.-S.; Jin, Y.; Liao, L.-S. Optimization of Low-Dimensional Components of Quasi-2D Perovskite Films for Deep-Blue Light-Emitting Diodes. *Adv. Mater.* **2019**, *31*, 1904319. [CrossRef]
6. Fakharuddin, A.; Gangishetty, M.K.; Abdi-Jalebi, M.; Chin, S.-H.; bin Mohd Yusoff, A.R.; Congreve, D.N.; Tress, W.; Deschler, F.; Vasilopoulou, M.; Bolink, H.J. Perovskite light-emitting diodes. *Nat. Electron.* **2022**, *5*, 203–216. [CrossRef]
7. Wang, H.; Sun, Y.; Chen, J.; Wang, F.; Han, R.; Zhang, C.; Kong, J.; Li, L.; Yang, J. A Review of Perovskite-Based Photodetectors and Their Applications. *Nanomaterials* **2022**, *12*, 4390. [CrossRef]
8. Lu, X.; Li, J.; Zhang, Y.; Han, Z.; He, Z.; Zou, Y.; Xu, X. Recent Progress on Perovskite Photodetectors for Narrowband Detection. *Adv. Photonics Res.* **2022**, *3*, 2100335. [CrossRef]
9. Miao, J.; Zhang, F. Recent progress on highly sensitive perovskite photodetectors. *J. Mater. Chem. C* **2019**, *7*, 1741–1791. [CrossRef]
10. Li, G.; Su, Z.; Li, M.; Lee, H.K.H.; Datt, R.; Hughes, D.; Wang, C.; Flatken, M.; Köbler, H.; Jerónimo-Rendon, J.J.; et al. Structure and Performance Evolution of Perovskite Solar Cells under Extreme Temperatures. *Adv. Energy Mater.* **2022**, *12*, 2202887. [CrossRef]
11. Schlipf, J.; Hu, Y.; Pratap, S.; Bießmann, L.; Hohn, N.; Porcar, L.; Bein, T.; Docampo, P.; Müller-Buschbaum, P. Shedding Light on the Moisture Stability of 3D/2D Hybrid Perovskite Heterojunction Thin Films. *ACS Appl. Energy Mater.* **2019**, *2*, 1011–1018. [CrossRef]
12. Mahmud, M.A.; Duong, T.; Peng, J.; Wu, Y.; Shen, H.; Walter, D.; Nguyen, H.T.; Mozaffari, N.; Tabi, G.D.; Catchpole, K.R.; et al. Origin of Efficiency and Stability Enhancement in High-Performing Mixed Dimensional 2D–3D Perovskite Solar Cells: A Review. *Adv. Funct. Mater.* **2022**, *32*, 2009164. [CrossRef]
13. Davy, M.M.; Jadel, T.M.; Qin, C.; Luyun, B.; Mina, G. Recent progress in low dimensional (quasi-2D) and mixed dimensional (2D/3D) tin-based perovskite solar cells. *Sustain. Energy Fuels* **2021**, *5*, 34–51. [CrossRef]
14. Zhou, Y.; Wang, J.; Luo, D.; Hu, D.; Min, Y.; Xue, Q. Recent progress of halide perovskites for thermoelectric application. *Nano Energy* **2022**, *94*, 106949. [CrossRef]
15. Pisoni, A.; Jaćimović, J.; Barišić, O.S.; Spina, M.; Gaál, R.; Forró, L.; Horváth, E. Ultra-Low Thermal Conductivity in Organic–Inorganic Hybrid Perovskite $CH_3NH_3PbI_3$. *J. Phys. Chem. Lett.* **2014**, *5*, 2488–2492. [CrossRef] [PubMed]
16. Liu, T.; Yue, S.-Y.; Ratnasingham, S.; Degousée, T.; Varsini, P.; Briscoe, J.; McLachlan, M.A.; Hu, M.; Fenwick, O. Unusual Thermal Boundary Resistance in Halide Perovskites: A Way To Tune Ultralow Thermal Conductivity for Thermoelectrics. *ACS Appl. Mater. Interfaces* **2019**, *11*, 47507–47515. [CrossRef] [PubMed]
17. Whitfield, P.S.; Herron, N.; Guise, W.E.; Page, K.; Cheng, Y.Q.; Milas, I.; Crawford, M.K. Structures, Phase Transitions and Tricritical Behavior of the Hybrid Perovskite Methyl Ammonium Lead Iodide. *Sci. Rep.* **2016**, *6*, 35685. [CrossRef] [PubMed]
18. Jacobsson, T.J.; Schwan, L.J.; Ottosson, M.; Hagfeldt, A.; Edvinsson, T. Determination of Thermal Expansion Coefficients and Locating the Temperature-Induced Phase Transition in Methylammonium Lead Perovskites Using X-ray Diffraction. *Inorg. Chem.* **2015**, *54*, 10678–10685. [CrossRef] [PubMed]

19. Liu, Y.; Yang, Z.; Liu, S. Recent Progress in Single-Crystalline Perovskite Research Including Crystal Preparation, Property Evaluation, and Applications. *Adv. Sci.* **2018**, *5*, 1700471. [CrossRef]
20. Conings, B.; Drijkoningen, J.; Gauquelin, N.; Babayigit, A.; D'Haen, J.; D'Olieslaeger, L.; Ethirajan, A.; Verbeeck, J.; Manca, J.; Mosconi, E.; et al. Intrinsic Thermal Instability of Methylammonium Lead Trihalide Perovskite. *Adv. Energy Mater.* **2015**, *5*, 1500477. [CrossRef]
21. Aristidou, N.; Sanchez-Molina, I.; Chotchuangchutchaval, T.; Brown, M.; Martinez, L.; Rath, T.; Haque, S.A. The Role of Oxygen in the Degradation of Methylammonium Lead Trihalide Perovskite Photoactive Layers. *Angew. Chem. Int. Ed.* **2015**, *54*, 8208–8212. [CrossRef] [PubMed]
22. Jia, Y.; Kerner, R.A.; Grede, A.J.; Brigeman, A.N.; Rand, B.P.; Giebink, N.C. Diode-Pumped Organo-Lead Halide Perovskite Lasing in a Metal-Clad Distributed Feedback Resonator. *Nano Lett.* **2016**, *16*, 4624–4629. [CrossRef] [PubMed]
23. Pipitone, C.; Boldrini, S.; Ferrario, A.; Garcìa-Espejo, G.; Guagliardi, A.; Masciocchi, N.; Martorana, A.; Giannici, F. Ultralow thermal conductivity in 1D and 2D imidazolium-based lead halide perovskites. *Appl. Phys. Lett.* **2021**, *119*, 101104. [CrossRef]
24. Abdul Ghani, I.B.; Khalid, M.; Hussain, M.I.; Hussain, M.M.; Ashraf, R.; Wang, J. Recent advancement in perovskite solar cell with imidazole additive. *Mater. Sci. Semicond. Process.* **2022**, *148*, 106788. [CrossRef]
25. Yao, Z.-S.; Guan, H.; Shiota, Y.; He, C.-T.; Wang, X.-L.; Wu, S.-Q.; Zheng, X.; Su, S.-Q.; Yoshizawa, K.; Kong, X.; et al. Giant anisotropic thermal expansion actuated by thermodynamically assisted reorientation of imidazoliums in a single crystal. *Nat. Commun.* **2019**, *10*, 4805. [CrossRef]
26. Smółka, S.; Mączka, M.; Drozdowski, D.; Stefańska, D.; Gągor, A.; Sieradzki, A.; Zaręba, J.K.; Ptak, M. Effect of Dimensionality on Photoluminescence and Dielectric Properties of Imidazolium Lead Bromides. *Inorg. Chem.* **2022**, *61*, 15225–15238. [CrossRef]
27. Guo, Y.-Y.; McNulty, J.A.; Mica, N.A.; Samuel, I.D.W.; Slawin, A.M.Z.; Bühl, M.; Lightfoot, P. Structure-directing effects in (110)-layered hybrid perovskites containing two distinct organic moieties. *Chem. Commun.* **2019**, *55*, 9935–9938. [CrossRef]
28. *TOPAS-R, v.3.0*; Bruker AXS: Karlsruhe, Germany, 2005.
29. Spek, A. LEPAGE—An MS-DOS program for the determination of the metrical symmetry of a translation lattice. *J. Appl. Crystallogr.* **1988**, *21*, 578–579. [CrossRef]
30. Dollase, W. Correction of intensities for preferred orientation in powder diffractometry: Application of the March model. *J. Appl. Crystallogr.* **1986**, *19*, 267–272. [CrossRef]
31. Williams, T.; Kelley, C.; Lang, R.; Kotz, D.; Campbell, J. Gnuplot v.5.4: An Interactive Plotting Program. 2021. Available online: http://www.gnuplot.info (accessed on 2 May 2023).
32. Tauc, J. Optical properties and electronic structure of amorphous Ge and Si. *Mater. Res. Bull.* **1968**, *3*, 37–46. [CrossRef]
33. Dursun, I.; De Bastiani, M.; Turedi, B.; Alamer, B.; Shkurenko, A.; Yin, J.; El-Zohry, A.M.; Gereige, I.; Al Saggaf, A.; Mohammed, O.F.; et al. CsPb2Br5 Single Crystals: Synthesis and Characterization. *ChemSusChem* **2017**, *10*, 3746–3749. [CrossRef] [PubMed]
34. López, C.A.; Abia, C.; Alvarez-Galván, M.C.; Hong, B.-K.; Martínez-Huerta, M.V.; Serrano-Sánchez, F.; Carrascoso, F.; Castellanos-Gómez, A.; Fernández-Díaz, M.T.; Alonso, J.A. Crystal Structure Features of CsPbBr3 Perovskite Prepared by Mechanochemical Synthesis. *ACS Omega* **2020**, *5*, 5931–5938. [CrossRef] [PubMed]
35. Stoumpos, C.C.; Frazer, L.; Clark, D.J.; Kim, Y.S.; Rhim, S.H.; Freeman, A.J.; Ketterson, J.B.; Jang, J.I.; Kanatzidis, M.G. Hybrid Germanium Iodide Perovskite Semiconductors: Active Lone Pairs, Structural Distortions, Direct and Indirect Energy Gaps, and Strong Nonlinear Optical Properties. *J. Am. Chem. Soc.* **2015**, *137*, 6804–6819. [CrossRef]
36. Stoumpos, C.C.; Mao, L.; Malliakas, C.D.; Kanatzidis, M.G. Structure–Band Gap Relationships in Hexagonal Polytypes and Low-Dimensional Structures of Hybrid Tin Iodide Perovskites. *Inorg. Chem.* **2017**, *56*, 56–73. [CrossRef]
37. Mitzi, D.B.; Wang, S.; Feild, C.A.; Chess, C.A.; Guloy, A.M. Conducting Layered Organic-inorganic Halides Containing <110>-Oriented Perovskite Sheets. *Science* **1995**, *267*, 1473–1476. [CrossRef] [PubMed]
38. Schueller, E.C.; Laurita, G.; Fabini, D.H.; Stoumpos, C.C.; Kanatzidis, M.G.; Seshadri, R. Crystal Structure Evolution and Notable Thermal Expansion in Hybrid Perovskites Formamidinium Tin Iodide and Formamidinium Lead Bromide. *Inorg. Chem.* **2018**, *57*, 695–701. [CrossRef] [PubMed]
39. McGovern, L.; Futscher, M.H.; Muscarella, L.A.; Ehrler, B. Understanding the Stability of MAPbBr3 versus MAPbI3: Suppression of Methylammonium Migration and Reduction of Halide Migration. *J. Phys. Chem. Lett.* **2020**, *11*, 7127–7132. [CrossRef] [PubMed]
40. Brunetti, B.; Cavallo, C.; Ciccioli, A.; Gigli, G.; Latini, A. On the Thermal and Thermodynamic (In)Stability of Methylammonium Lead Halide Perovskites. *Sci. Rep.* **2016**, *6*, 31896. [CrossRef] [PubMed]
41. Ohashi, Y. A program to calculate the strain tensor from two sets of unit-cell parameters. In *Comparative Crystal Chemistry*; Hazen, R., Finger, L., Eds.; Wiley: New York, NY, USA, 1982; pp. 92–102.
42. Kaminski, W. WinTensor, v.1.5. 2014. Available online: http://www.wintensor.com (accessed on 18 April 2023).